A study on the background and clustering seismicity in the Taiwan region by using point process models

Jiancang Zhuang[1], *Chung-Pai Chang*[2], *Yosihiko Ogata*[1] *and Yuh-Ing Chen*[2]
[1]*Institute of Statistical Mathematics, 4-6-7 Minami Azabu, Minato-Ku, Tokyo 106-8659, Japan*
[2]*Institute of Statistics, National Central University, Chung-Li, Taiwan, ROC*

October 1, 2004

Abstract

[1] This paper investigates the shallow seismicity in the Taiwan region during the 20th century using the stochastic declustering method, which is developed based on the theory of the epidemic type aftershock sequence (ETAS) model. It provides a probability based tool to objectively separate the space-time occurrences of earthquakes into a background and a clustering component. Based on the background and clustering seismicity rates, we discuss the correlation between the distribution of the cluster ratio and regional seismotectonic structures. Especially, the areas of the highest clustering ratio correspond to the major strike slip fault traces in and around Taiwan. The outputs for the stochastically declustered catalogue also show a clear quiescence during 1960–1990 in the background seismicity in the Taiwan inland preceding the recovery of activation and the occurrences of the 1999 Chi-Chi earthquake of M_L7.3, while the other active regions show the stationary background activity. This could be interpreted as the effect of the aseismic slip in the Chichi rupture fault, by which the inland region around the Chi-Chi source becomes stress-shadow.

1 Introduction

[2] Located on the convergent boundary between the Eurasian and the Philippine

Sea plates, Taiwan is one of the most active seismic regions in the world. In the 20th century, disastrous earthquakes have caused huge damages to properties as well as to human lives in this region [see, e.g., *Hsu*, 1961; *Tsai*, 1985; *Wang and Kuo*, 1995; *Wang*, 1998]. It is of importance to recognize the background seismicity in the Taiwan region for the purpose of future earthquake hazard evaluation. On the other hand, large aftershocks may also postulate significant hazards as their mainshocks, especially in populated areas, where and when the buildings have already been weaken by the main shock. This is among the reasons why it is important to assess the seismic hazard, caused by mainshocks and aftershocks. To estimate the background seismicity hazard and to characterize the earthquake clusters, a proper separation of the background seismicity from the total seismicity is necessary.

[3] In the next section, we present the the motivation for proposing probability based declustering method, and then give a brief description of the space-time ETAS model and the stochastic declustering method. In Section 3, we introduce the tectonic background of the Taiwan region and the selection of the data in the analysis. In Sections 4 to 7, we use this model-based declustering method as a basic tool to obtain the background seismicity and clustering seismicity in the Taiwan region during the period 1900–1999, and to describe their relation to the seismotectonic features in various important subregions in Taiwan. Also, we will discuss temporal seismicity rate changes during the century with the special reference to the 1999 Chi-Chi earthquake.

2 Modelling

2.1 Why stochastic declustering

[4] Declustering is one of the most important and frequent issues in the seismicity study. Seismicity is known to be clustered in both space and time. The earthquake clusters always complicate the statistical analysis of the seismic background variation that might be related to the stress changes in the tectonic environments. Moreover, the

overlap of these clusters with each other causes difficulties in the analysis of these clusters themselves. On the other hand, there is a great need of intensive studies of earthquake clusters. For the purpose of long-term earthquake prediction, a good estimate of the background seismicity rate is necessary, in which temporal and spatial clustering in the earthquake catalogue should be removed.

[5] Earthquake cluster features differ from place to place, and give different impressions the seismologists, who, thus, have proposed quite a number of declustering methods. These methods can be classified into two classes: window-based and link-based. The window-based methods decluster an earthquake catalogue by removing the smaller earthquakes in a space-time window around a larger event (identified as the mainshock) [see, e.g., *Utsu*, 1969; *Gardner and Knopoff*, 1974]. Usually, the larger is the mainshock magnitude, the bigger the window size. The link-based methods remove the events which are within a compromised space-time distance to an earlier event [*Reasenberg*, 1985; single-link clusters, see, *Frohlich and Davis*, 1990; *Davis and Frohlich*, 1991].

[6] In these conventional declustering methods, it is difficult to find optimal parameters for the sizes of space-time windows or the link distance and, currently, they are chosen from the experience of the researchers. Thus the declustering output may be quite sensitive to such subjective choices. This is among the reasons why there have been so many declustering methods. Another reason for the existence of so many declustering methods is that our uncertainty to the underground earthquake processes results in the fuzziness of the concept of aftershock.

[7] Another shortcoming of the conventional declustering is that removing earthquakes in the catalogue may cause losses of potential useful information. A more reasonable way is to use a model to quantify the observed data, and then use these quantified observations to test the hypotheses on seismicity and evaluate its confidence level.

[8] Most of the statistical models for the space-time-magnitude occurrences of earthquake clusters are in the form of branching point process [*Kagan*, 1991; *Musmeci and*

Vere-Jones, 1992; *Rathbun*, 1993; *Ogata*, 1998; *Ogata et al.*, 2003, 2004; *Zhuang et al.*, 2002, 2004; *Console and Murru*, 2001; *Console et al.*, 2002]. In general, these models classify the seismicity into two components, the background and the cluster, where each earthquake event, no matter if it is from the background component (usually assumed to be a space-time Poisson process, stationary or non-stationary, homogeneous or non-homogeneous) or generated by another event, produces (triggers) its own offspring (aftershocks) according to some branching rules. In the models mentioned above, *Musmeci and Vere-Jones* [1992], *Ogata* [1998], *Zhuang et al.* [2002, 2004] and *Console et al.* [2003] considered to use spatially inhomogeneous background rates in the model. *Musmeci and Vere-Jones* [1992] assume the background seismicity was proportional to a kernel estimate obtained from spatial location of all the earthquakes including clusters. *Ogata* [1998] used a conventional declustering method for a preliminary estimation of the background rate by fitting bi-cubic B-spline functions before fitting to model. *Console et al.* [2003] firstly divided the study region into many cells, then set the smoothed values at each node by averaging the number of events in the neighboring cells. To avoid pre-setting the background rate, *Zhuang et al.* [2002, 2004] used an iterative approach to simultaneously estimate the background seismicity rate and the parameters associated with the clustering structures, where the background seismicity is estimated by weighted variable kernel functions. An alternative is to use Bayesian analysis with smoothness prior for the background rates as well as for other parameters [*Ogata et al.*, 2003, 2004].

[9] To obtain an objectively declustered catalogue, *Zhuang et al.* [2002, 2004] proposed the stochastic declustering method as the alternative to the conventional methods. In this method, it is not deterministic any more whether an earthquake is a background events or triggered by another. Instead, each event has a probability to be either a background event or an direct offspring triggered by others. The main task of the stochastic declustering algorithm is to estimate this probability for each event according to some models for describing earthquake clustering features.

2.2 Space-time epidemic type aftershock models

[10] Several authors have proposed different forms of point process model for the space-time clustering seismicity rate [*Ogata*, 1998; also see *Ogata*, 1988, 1992; *Kagan*, 1991; *Musmeci and Vere-Jones*, 1992; *Rathbun*, 1993; *Console and Murru*, 2001; and *Console et al.*, 2002]. These models are represented in terms of a conditional intensity function for seismicity rate in time, space and magnitude (see *Daley and Vere-Jones* [2002], Chap. 7, for mathematical details on the conditional intensity function) that is formally defined by

$$\lambda(t, x, y, M|\mathcal{H}_t) = \frac{\mathbf{E}\{N(dt\,dx\,dy\,dM)|\mathcal{H}_t\}}{dt\,dx\,dy\,dM} \tag{1}$$

where $\mathbf{E}\{\cdot\}$ represents the average over an infinite number of realizations of the process at a particular time t, a location (x, y) and a magnitude M with the provided occurrence history $\mathcal{H}_t$ up to time t. The mathematical term "conditional intensity" means "occurrence rate of events conditional on the observation history of the previous events", and hereafter we call it seismicity rate. The seismicity rate function of these models can be written in the common form of

$$\lambda(t, x, y, M|\mathcal{H}_t) = J(M)\left[\mu(x, y) + \sum_{i:t_i<t} \xi(t - t_i, x - x_i, y - y_i; M_i)\right], \tag{2}$$

where the background seismicity rate $\mu(x, y)$ is a function of space, but not of time. The contribution to the seismicity ratre of an earthquake with a magnitude M, $\xi(t, x, y; M)$, has been assigned the several forms by different authors. *Musmeci and Vere-Jones* [1992] uses a diffusion type response functions. In most of other recent studies, $\xi(t, x, y; M)$ takes or can be represented by a separable form,

$$\xi(t, x, y; M) = \kappa(M)g(t)f(x, y; M) \tag{3}$$

where $\kappa(M)$ can be regarded as the expected number of events triggered by an event of magnitude M, and the function g and f are normalized, such that $\int g(t)dt = 1$ and

$\iint f(x,y;M)dxdy = 1$, representing the probability density function (p.d.f.) of the occurrence time and location of a direct offspring event, respectively. *Rathbun* [1993], *Ogata* [1998] and *Console* [2003] took the form

$$\kappa(M) = Ae^{\alpha(M-M_C)}, \tag{4}$$

and,

$$g(t) = \frac{p-1}{c}\left(1+\frac{t}{c}\right)^{-p}, \tag{5}$$

which is the p.d.f. form of the modified Omori law [*Utsu*, 1969]. For the spatial p.d.f., $f(x,y;M)$, the following different functions have been used,

Model 1 [*Rathbun*, 1993; *Console et al.*, 2003]

$$f(x,y;M) = \frac{1}{2\pi D^2}e^{-\frac{x^2+y^2}{2D^2}}; \tag{6}$$

Model 2 [*Ogata*, 1998; *Zhuang et al.*, 2002]

$$f(x,y;M) = \frac{1}{2\pi D^2 e^{\alpha(M-M_C)}}e^{-\frac{x^2+y^2}{2D^2e^{\alpha(M-M_C)}}}, \tag{7}$$

where the parameter α is the same one as in (4);

Model 3 [*Ogata*, 1998; *Console et al.*, 2003]

$$f(x,y;M) = \frac{q-1}{\pi D^2}\left(1+\frac{x^2+y^2}{D^2}\right)^{-q}; \tag{8}$$

Model 4 [*Ogata*, 1998; *Zhuang et al.*, 2002, 2004]

$$f(x,y;M) = \frac{q-1}{\pi D^2 e^{\alpha(M-M_C)}}\left(1+\frac{x^2+y^2}{D^2e^{\alpha(M-M_C)}}\right)^{-q}; \tag{9}$$

and in this paper, we also consider

Model 5 [*Ogata and Zhuang*, 2004]

$$f(x,y;M) = \frac{q-1}{\pi D^2 e^{\gamma(M-M_C)}}\left(1+\frac{x^2+y^2}{D^2e^{\gamma(M-M_C)}}\right)^{-q}, \tag{10}$$

where γ is an independent parameter from α.

[11] Central arguments on the optimal choice among (6)-(10) are: (a) Do aftershocks decay in a short range or long range? (b) Is the aftershock region scaled with the main-shock magnitude? (c) If so, is its scale law the same as for the expected number of events? *Ogata* [1998], *Console et al.* [2002] and *Zhuang et al.* [2004] all showed that the aftershocks decay in a long range in different studies. In (6) and (8), the spatial scaling factor has the same exponent as the expected number of offspring events in (4). This is consistent with the conclusion of *Yamanaka and Shimazaki* [1990, Equation (10)]. But *Zhuang et al.* [2004] found that the above two exponents should be different. Thus we also adopt the new model as in (10).

[12] The p.d.f. for the magnitude distribution is

$$J(M) = \beta \exp[-\beta(M - M_C)], \qquad M \geq M_C, \tag{11}$$

where the parameter β is linked to the Gutenberg-Richter's b-value by

$$\beta = b \log 10. \tag{12}$$

[13] Since the magnitude distribution is independent of other components and could be separated from the full joint likelihood of magnitudes and occurrences time and space, (2) can be separated by the following space-time seismicity rate function

$$\lambda(t, x, y|\mathcal{H}_t) = \mu(x, y) + \sum_{i:t_i<t} \kappa(M_i) g(t - t_i) f(x - x_i, y - y_i|M_i). \tag{13}$$

2.3 Maximum likelihood estimates and model selection

[14] Given a set of observed earthquake data $\{(t_i, x_i, y_i, M_i) : i = 1, 2, \ldots, N\}$, if the background rate $\mu(x, y) = \nu u(x, y)$ where $u(x, y)$ is known, parameters in (13) can be estimated by maximizing the log-likelihood [cf. *Daley and Vere-Jones*, 2003, Chap. 7]

$$\log L(\boldsymbol{\theta}) = \sum_{j:(t_j,x_j,y_j)\in S\times[T_1,T_2]} \log \lambda(t_j, x_j, y_j|\mathcal{H}_{t_j}) - \iint_S \int_{T_1}^{T_2} \lambda(t, x, y|\mathcal{H}_t) dt\, dx\, dy, \tag{14}$$

where $\boldsymbol{\theta} = (\nu, A, \alpha, c, p, D)$ for Models 1 and 2, $\boldsymbol{\theta} = (\nu, A, \alpha, c, p, D, q)$ for Models 3 and 4, and $\boldsymbol{\theta} = (\nu, A, \alpha, c, p, D, q, \gamma)$ for Model 5, and j runs over all the events in the study region S and time period $[T_1, T_2]$. Because the events, especially large ones, outside the study region or before the study time period can also trigger seismicity inside the study region and time period, we include these events in the observation history $\mathcal{H}_t$ and call them *complemental events*, while the events inside the study space-time ranges are called *target events*. Thus, the complemental events only contribute to the seismicity rate function, but not be included in the summation in the right-hand-side of (14), i.e., the subscript i runs over all the events in the catalogue in (2) while j in (14) runs over only the target events in the space-time ranges $S \times [T_1, T_2]$ of interest. *Zhuang et al.* [2002] pointed out that at least the information on the complemental large earthquakes should be included in the history if their contribution is substantial to the seismicity rate of the target events.

[15] The goodness-of-fit comparison between the above five models, can be carried out by using the Akaike Information Criterion (AIC, see Akaike 1974). The statistic

$$AIC = -2 \max_{\boldsymbol{\theta}} \log L(\boldsymbol{\theta}) + 2k_p \tag{15}$$

is computed for each of the models fitted to the data, where k_p is the total number of fitted parameters. The model with lower AIC value is taken as giving better choice for forward prediction purpose. Furthermore, the AIC can be used as a rough guide to testing a model with $k + d$ parameters against a null model with just k parameters. We take a difference of 2 in AIC values as a rough estimate of significance level of 5%. If standard asymptotics are applied, such a difference corresponds to a significance level of 4.6% when $d = 1$, 5.0% when $d = 2$, 4.6% when $d = 3$, and 3.5% when $d = 5$.

2.4 The thinning method and stochastic declustering

[16] The technical key point of the stochastic declustering method is the thinning operation to a point process (i.e., random deletion of points, c.f. *Lewis and Shedler*, 1979;

Ogata, 1981; *Daley and Vere-Jones*, 2003). Observe (13), the relative contribution of a previous ith event to the total seismicity rate at the occurrence time and location of the jth event, (t_j, x_j, y_j), is

$$\rho_{ij} = \begin{cases} \zeta_i(t_j, x_j, y_j)/\lambda(t_j, x_j, y_j|\mathcal{H}_{t_j}), & \text{when } j > i, \\ 0, & \text{otherwise,} \end{cases} \tag{16}$$

where

$$\zeta_i(t, x, y) = \kappa(M_i)g(t - t_i)f(x - x_i, y - y_i|M_i), \tag{17}$$

represents the rate triggered by the ith event. That is to say, for each $j = 1, 2, \ldots, N$, if we select the jth event with probability ρ_{ij}, we can realize a subprocess of the events being the direct offspring of the ith event. In this way, ρ_{ij} can be naturally regarded as the probability of the jth event being a direct offspring of the ith event. Furthermore, the probability of the event j being a background event is

$$\varphi_j = \frac{\mu(x_j, y_j)}{\lambda(t_j, x_j, y_j|\mathcal{H}_{t_j})}. \tag{18}$$

and the probability that the jth event is triggered is given by

$$\rho_j = 1 - \varphi_j = \sum_i \rho_{ij}, \tag{19}$$

In other words, if we select each event j with probabilities φ_j, we can then form up a new processes being the background subprocess with a rate function $\mu(x, y)$, and its complement being the clustering subprocess.

[17] A stochastic declustered catalogue produced from the above procedures is not unique, because it depends on the random numbers used in the selection of events to form the background seismicity. This method gives the probabilities how likely each event is a background event or triggered by other events, but not makes a fixed judgment on whether an event is an aftershock or not. This should be considered an advantage of the method, because it allows uncertainty about the declustering to be quantified. By repeating random selection, we can easily produce many copies of the declustered catalogue, from which we

can evaluate the uncertainty or significance of a particular feature associated with the declustered catalogue.

2.5 Variable kernel estimates of seismicity rates

[18] The total spatial seismicity rate can be estimated by using variable kernel estimates

$$\hat{m}(x,y) = \frac{1}{T}\sum_j Z_{h_j}(x-x_j, y-y_j), \tag{20}$$

where T is the length of the time period of the process, subscript j runs over all the event in the process and Z is the Gaussian density function [*Zhuang et al.*, 2002]. The variable bandwidth h_j (the standard deviation of the Gaussian density) is determined by

$$h_j = \max\{\epsilon, \inf(r:\ N[B(x_i, y_i; r)] > n_p)\}, \tag{21}$$

where ϵ is the allowed minimum bandwidth, $B(x, y; r)$ is the disk of radius r centered at (x, y), and n_p is a positive integer, i.e., h_j is the distance to its n_pth closest neighbor.

[19] Once the thinning probabilities $\{\varphi_j\}$ are obtained, we can estimate the spatial background seismicity rate by using weighted variable kernel estimates [*Zhuang et al.*, 2002],

$$\hat{\mu}(x,y) = \frac{1}{T}\sum_j \varphi_j Z_{h_j}(x-x_j, y-y_j), \tag{22}$$

where T, Z and h_j are defined as in (20). Equation (22) is equivalent to the average of kernel estimates for the spatial seismicity rate in many realizations of the background catalogues produced by using the thinning method (stochastic declustering), i.e.,

$$\hat{\mu}(x,y) = \mathbf{E}\left[\frac{1}{T}\sum_j X_j Z_{h_j}(x-x_j, y-y_j)\right], \tag{23}$$

where the random variables, X_j, $j = 1, \cdots, N$, independently takes values 1 or 0 with probability φ_j and $1-\varphi_j$, respectively, and $\mathbf{E}[\cdot]$ represents the average over infinite combinatorial realizations of $\{X_j;\ j = 1, 2, \cdots N\}$.

[20] Simply take the difference between the total seismicity rate and the background seismicity rate, and we can get the estimate of the clustering rate function, i.e., the estimate of the clustering rate is

$$\hat{C}(x,y) = \hat{m}(x,y) - \hat{\mu}(x,y) = \frac{1}{T}\sum_j (1-\varphi_j) Z_{h_j}(x-x_j, y-y_j), \tag{24}$$

To show the degree of clustering, we also define the clustering ratio function as the ratio of the clustering seismcity rate to the total seismicity rate,

$$\Omega(x,y) = \frac{\hat{C}(x,y)}{\hat{m}(x,y)}. \tag{25}$$

[21] The problem of optimal selection of n_p for the variable bandwidth for the statistics in (20), (22) and (24) can be solved in the following way. Remembering that the integral of the clustering term on the right side of (13) with respect to time,

$$I(x,y) = \frac{1}{T}\int_0^T \sum_{i:t_i<t} \kappa(M_i) g(t-t_i) f(x-x_i, y-y_i; M_i) dt \tag{26}$$

also provides an image of the clustering seismicity rate in space, but not so smoothed, we can in principle select a suitable n_p by minimizing the discrepancy between the low-frequency (smoothed) component of $I(x,y)$ in (26) and $\hat{C}(x,y)$ in (24). In practice, because the estimates are rather insensitive to the choice of n_p, a rough estimate is generally sufficient.

2.6 Algorithm for simultaneously estimating the background seismicity rate and model parameters

[22] The background seismicity and the parameters can be determined in the clustering structures simultaneously by an iterative approach [*Zhuang et al.*, 2002, 2004]. Firstly, we assume some initial background seismicity rate, using the maximum likelihood procedure to get the parameters in the branching structure. Then calculate the background probabilities $\{\varphi_j : j = 1, 2, \cdots N\}$ for all of the events by using (18). Substitute these φ_j into (22) to get a better estimate of the background seismicity rate. Use this newly estimated

background seismicity rate to replace the initial background rate, and repeat these steps for many time, until the results converge.

[23] This algorithm converges quickly, usually in 5∼20 steps. *Zhuang et al.* [2002] showed that for the central New Zealand catalog of shallow earthquakes, the algorithm converged within 10 steps.

3 Tectonic background and data select

3.1 Tectonic background

[24] The Taiwan island is located at the junction between two subduction systems. On the east, the Philippine Sea plate (PH) subducts along the Ryukyu subduction system, northward beneath the Eurasian plate (EU). On the south, the Philippine Sea plate overrides the crust of the South China Sea at the Manila trench (Fig. 1). According to GPS observations, the convergent rate between the northern Luzon volcanic arc (NLA in Fig. 1a), which is located on the Philippine Sea plate, and the southeast Eurasian continental margin is about 8.2 cm/yr with a azimuth of 310° [*Yu et al.*, 1997].

[25] The general structural trends of the Taiwan mountain belt show an elongate S-shape. As a result of regional compression, the Taiwan island consists of several provinces [*Ho*, 1986] with a main structural grain that tend approximately along the NNE direction (Fig. 1a). From west to east, they are: the Coastal Plain, the Western Foothills, the Hsüehshan Range, the Central Range, and the Coastal Range. The Coastal Plain, Western Foothills and Hsüehshan Range in the western Taiwan are composed of thick sequences of Cenozoic shallow-marine siliciclastics. The Western Foothills and Hsüehshan Range are deformed by a combination of folds and thrust faults, which trend mainly northeast or north and dip toward the east or southeast [*Suppe*, 1980; *Ho*, 1986]. The basement of Central Range is composed of the pre-Tertiary complex affected by Neogene greenschist facies and higher grades of polyphase Mesozoic-Cenozoic metamorphism. East of the Central Range, the Coastal Range is mainly composed of Neogene andesitic volcanic

units and associated flyschoid and turbidite sediments, which belongs to the Philippine Sea plate [*Ho*, 1986] and represents a section of the Luzon arc that is being accreted onto the Eurasian continent (Fig. 1). It is worthwhile to mention that the suture zone between the eastern Central Range and the Coastal Range, the Longitudinal Valley, is also one of the most active deformation zones in Taiwan [*Tsai*, 1986; *Yu et al.*, 1997].

[26] From the distribution of seismicity, *Tsai et al.* [1977] divided the boundary between the Eurasian and Philippine Sea plates in Taiwan area into three segments. Generally, we follow their suggestion, but our division differs because we consider also the regional tectonic background. In this study, the Taiwan region is divided into 3 seismotectonic zones; they are: (I) the Western subregion, including the Taiwan Strait, Coastal Plain, the Western Foothills, the Hsüehshan Range and the Central Range ; (II) the Northeastern Subregion, i.e., the Ryukyu subduction system; (III) the Southeastern subregion, including the Coastal Range and the Philippine Sea plate (Fig. 1).

3.2 Data selection

[27] The history of the monitoring network in Taiwan can be mainly divided into several periods [*Wang*, 1998]: (a) From 1897 on, 3-component low-gain displacement seismometers were installed in the Taiwan region by Japanese seismologists during the period 1897-1935. Because of non-synchronous timing system, remarkable errors for arrival times results in high errors in earthquake locations; some acceleration seismometers and strong-motion seismometers were put into use in 1951; in 1963, a World Standard Network station was constructed in Anpu equipped with two high-gain electric-record seismometers, one of long-period and one of short-period.; (b) Taiwan Telemetered Seismographic Network (TTSN) of 24 stations was constructed from 1972, each station equipped with a 3-component high-gain and analog velocity seismometer; and (c) Since 1991, Taiwan Seismic Network (TSN) upgraded from the old CWB (Central Weather Bureau) seismic network, which consists of 72 stations, each equipped with 3-component digital velocity seismometers.

[28] A complete and homogeneous earthquake catalogue is important for the ETAS fitting. Taking the above discussion into consideration, we take the target events of $M \geq 5.3$ and depths ≤ 55 km in the period from 1941-1-1 (14975 days from 1900-1-1) to 2001-12-31 and in the region (120∼122°E, 22∼25°N; see Figure 2a) for estimating the parameters, the events with a magnitude no less than 5.3 outside the target region and period are used as the complementary events, i.e., they do not directly contribute to the likelihood function, but influence the seismicity rate function (cf., Section 2.3).

4 Parameters and spatial intensities of the background and clustering seismicity

[29] According to the principle in Section 2.5, we use $n_p = 3$ and $\epsilon = 0.05\ deg$ in the variable kernel estimates of the background rate, where $1deg \approx 111.1$ km, meaning 1/360 of the great arc of the earth surface, approximated by a sphere. The estimated parameters for the branching structures of the five models listed in Table 1. Among these models, Model 5 is chosen as the best fit to the Taiwan data, which against confirms the following conclusions on the spatial distribution of directly triggered events: (a) the triggered events decay in a long range decay rather than a short range decay; (b) aftershock region is scaled by an exponential law of the magnitude of the ancestor event; (c) the above spatial scaling law is not the same as the exponential law for the expected number of events.

[30] The AIC values indicate that Models 1 and 3 fit the data better than Models 2 and 4, respectively. This does not imply that the aftershock region showed be scaled by a constant. The reason why this holds is that the difference between the exponents α and γ is too large. That is to say, if the two exponents differ not so much from each other, Models 2 and 4 would be better than Models 1 and 3, respectively. Comparing to Models 1 and 3, simply assuming that the two exponential laws take the same exponents may lead to the wrong conclusion that scaling the aftershock region is unnecessary. Indeed, the minimum AIC attained by Model 5 supports the spatial scaling by the magnitude of

the direct ancestor.

[31] In evaluating the spatial variations of the total seismicity rate, the background seismicity rate, clustering seismicity rate and clustering ratio, we extend the calculation over a larger region, (N21.5 $\sim$ 25.2°, E120 $\sim$ 123°), than the study region, (N22 $\sim$ 25°, E120 $\sim$ 122°), with the parameters from fitting Model 5 to the data of events only falling in the study space-time range. The distributions of the above variables, as shown in Figures 3, indicate the followings:

(a) **Total seismicity rate.** As shown in logarithm scale in Figure 3(a), the biggest contribution to the total seismicity rate is from the convergence part on the plate boundaries. The most active region is on the northern part of the convergence line, where the Philippine plate subducting underneath the Eurasian plate. The total seismicity rate decreases with distances from the convergence lines. But the total seismicity rate is relatively low in the middle inland region such as the Hsüehshan Range. The western inland areas has several local maxima in the total seismicity rate, caused by several big earthquake sequences or swarms.

(b) **Background seismicity rate**. Estimated by using (22) to remove the clustering components, the background seismicity rate dose not vary so much as the total seismicity rate does. The high values of the background seismicity rate distribute along the convergence line between the colliding of Philippine and Eurasian plates and off the east coast of the Taiwan Island. Overall the high background seismicity rate show a pattern of belts, which distributes parallel to the tectonic structure lines.

(c) **Clustering seismicity rate**. The clustering seismicity rate contains most of the irregular components of the total seismicity because the background part is taken away. The absolute values of highest clustering seismicity along the Ryukyu Trench are much higher than in other regions.

(d) **Clustering ratio**. This appears largely different from the above variations. The rates of both background and clustering seismicity are both high along the Ryukyu Trench, but clustering ratio changes dramatically. The clustering ratio is high in western part but very low on the eastern part. In the northwestern inland areas, the background seismicity rate is much lower than in the northeastern subregion, but higher clustering ratio implies that it is not so easy to have an earthquake inside, but that, once a large earthquake occurs, it is followed by a large number of aftershocks with very high probability. Furthermore, the asperities of the fault are expected to be in the region of the low clustering ratio but next to the high background and high clustering ratio [cf. *Ogata*, 2004]. These features should be considered for the evaluation of the losses caused by future earthquakes. The seismicity in the southwest inland region is less clustering, but still shows the similar feature. This difference from the northwest inland region may be caused by the geological properties of regional crustal materials, as shown in Figure 1.

5 Interpretation of the high clustering ratio regions by the tectonic structures

[32] As mentioned in the previous sections, the distribution of seismicity of the Taiwan area can be explained largely by the convergent tectonic framework between the Eurasian and Philippine Sea plates. Nevertheless, the spatial variation of the clustering ratio reveals a more complex pattern different from the seismic rates. For example, around the eastern distal part of the Ryukyu Trench, both background and clustering seismicity are of high rate, but the clustering ratio of this area is very low (Figures 3 and 4). The significance of our calculated clustering ratio must be discussed in this section.

[33] At the first approximation, four areas of high clustering ratio cans be recognized around the Taiwan island; they are (a) the central-western Taiwan area, (b) the south-western Taiwan area, (c) the eastern Taiwan area, and (d) the southeastern Taiwan area

(Fig. 4). Comparison of the pattern of the clustering ratio with local tectonic background shows that the first two areas seem to have close geometrical correlations with so-called oblique structures within the Taiwan Foothills proposed by previous studied [e.g., *Ho*, 1979, 1986; *Pelletier and Stephan*, 1986; *Deffontaines et al.*, 1997]. In the western Taiwan, the Foothills display active asymmetric folds and low-angle thrust faults, fold axes trend mainly N20°E and have steep to overturned western flanks commonly cut by WNW vergent thrust faults. However, based on subsurface data [e.g., *Sun*, 1963, 1964], satellite images (SPOT), digital elevation models (data after Taiwan Forestry Bureau), SLAR images, aerial photographs and local field work, *Deffontaines et al.* [1994, 1997] have recognized a series of structures trending mainly N140°E oblique to the fold-and-thrust belt in the Western Foothills. They believed that these N140°E-trending structures correspond to transfer faults, that is to strike-slip faults parallel to the thrust transport direction which separate two parts of a given thrust sheet, each of which may have different displacements and deformations [*McClay*, 1992]. Among these transfer faults there are two most important zones can be defined: the Sanyi and the Chiayi transfer fault zones. These two transfer fault zones display also a high seismic activity; the distribution of earthquakes and the related focal mechanisms confirm the left-lateral movement along N140°E directions. Our studied result shows that in western Taiwan the clustering ratio around the Sanyi and the Chiayi transfer fault zones is much higher than that of other areas (Fig. 4). This phenomenon provides us very important information to explain the effect of seismic clustering.

[34] For further examining the relationship between the seismic clustering ratio and the regional tectonic framework, we pay attention to the area of eastern Taiwan. East of Taiwan, the area connects the Ryukyu Trench and the northern tip of Longitudinal Valley (Area III in Figure 4) displays also high clustering ratio. Although the structural pattern in this transition area is very complex, the transcurrent faults are the most obvious structures [*Lallemand and Liu*, 1998]. As the result of stress portioning, the westernmost

segment of Ryukyu accretionary wedge has been dragged toward the Taiwan island and formed this series of major right-lateral fault [*Dominguez et al.*, 1998; *Lallemand et al.*, 1999]. The observation from this area further leads us to believe that the clustering ratio has very close relationship with the strike-slip structure.

[35] The last area with high clustering ratio around the Taiwan island is in the southeastern offshore Taiwan. The tectonic background of this area is still not clear. This area runs eastward along the axis of a submarine canyon, which merges with the Taitung Canyon Fault Zone (TCFZ) near the Ryukyu trench (Fig. 4). Based on seismic observations, morphological feature, and magnetic anomaly, *Kao et al.* [2000] identified that the TCFZ is a large-scale right-lateral strike-slip fault. Moreover, they suggested that this fault system probably has repeatedly changed its position in response to the propagation of Taiwan's arc-continental collision. In other words, the current TCFZ must be a recently developed structure and will be abandoned once the transition migrates farther to the southwest. Their proposition implicates that there may be some strike-slip fault traces at the north of the TCFZ and our studied result provides a possible candidate for this model. Actually, the clustering ratio along the TCFZ is also high and confirms us again in our previous observations.

6 Stochastic declustering output and background seismicity

[36] Figure 3 gives the spatial variation of the background rates, based on the model formulation that it is stationary in time but nonhomogeneous in location. In fact, background seismicity often departure from stationarity, which may by influenced by changes of regional tectonic stress field. To understand how the background seismicity changes with, we can use the thinning procedure as mentioned in Section 2.3 to realize different stochastic version of declustered catalogues to detect the existence of changes of occurrence rates in these catalogues. Figure 2(c) show the epicenter maps and space-time plot

of an example version of the background catalogues. It seems that there is a quiescent period in the background seismicity around the source of the 1999/9/21 Chi-Chi earthquake (M_S7.9) from mid 1950s to mid 1990s, while the background occurrence rate in the eastern areas seems to be stationary. Similar patterns can be also find in the space-time plot for all of the events (Figure 2b). But the stationarity of the background catalogue cannot be easily figured out in eastern parts (projection distance more 130 km from Location A).

[37] To discuss how the background seismicity changes with time in the next section, we can use the thinning procedure as mentioned in Section 2.3 to realize different stochastic versions of declustered catalogs and then detect the existence of changes of occurrence rate in them. However, the direct way is to calculate the cumulative background seismicity,

$$S(t) = \sum_{t_i<t} \varphi_i, \tag{27}$$

where φ_i is the background probability defined in (18), and i runs over the events in some specified region. Similarly, the cumulative clustering seismicity can be evaluated by

$$C(t) = \sum_{t_i<t} (1 - \varphi_i). \tag{28}$$

If the model fits the seismicity well or the background occurrence rate is a constant function of time, the function $S(t)$ defined by (27) increases approximately in a constant rate with the time t. If the slope of $S(t)$ decreases, we call it quiescence in background seismicity, or simply background quiescence; otherwise, if the slope of $S(t)$ increases, we call it an activation in the background seismicity, or simply background activation.

7 An interpretation of the seismicity patterns preceding the Chi-Chi earthquake

[38] It may be worthwhile to provide here a speculation of aseismic slips may have taken place somewhere in or around the fault of the 1999 Chi-Chi earthquake that could change the Coulomb's stress failures. Then, this would make the quiescence in the background

activity in the stress-shadow regions, but remain active in other regions. In order to make a quantitative scenario owing to the *change of the Coulomb Failure Stress* (ΔCFS) we rely on the simple preliminary model of the Chi-Chi rupture adopted by *Yoshioka* [2001], which further provides detailed coseismic slip distribution on the fault plane by geodetic data inversion based on the GPS displacement data, taking account of the shape of the surface rupture and the centroid moment tensor solutions; that is, the fault size of 70 km×50 km, a dip angle of 31° and strike of N9°E, leading to the average coseismic slip and direction of 5.1m and N55°W (the rake angle 64°), respectively. We here assume the aseismic slip zone on the deeper half of the fault plane of the source. Explicitly stating for the calculation, we assume the same fault length and angles for the aseismic slip as those of the main rupture, but assume that the fault top is 12.5 km depth, fault width is 25 km, and the slip size is tentatively given as 10% (≈ 50 cm) as much as the estimated one for the main rupture.

[39] Seismicity regions in and around Taiwan are classified roughly into three regions by taking account local tectonic structures and the hypocenter distributions. The first region is far offshore of the northern half of Taiwan Island (Region A) included in the region IV of Figure 1. The seismicity here is mostly interplate earthquakes beneath Eurasian plate where Philippine Sea Plate is subducting northward along the Ryukyu Trench. Therefore, we consider the receiver fault angles of (strike, dip, rake) = (270°, 30°, 90°). The pattern of the ΔCFS values in this region at the depth of 30 km is given in Figure 5a. These are small but positive in all depth-range down to 50 km. The background seismicity in this region, given in Figure 6b, shows slightly increasing activity after 1940's, but this may be due to the improvement of detection rate of $M5.5$ events or more in such an offshore region from the land. At least, we see the steady activity after 1940's till the present.

[40] The second region is the eastern offshore of the LV (Region B) included in the Region V. The dominating earthquake mechanism here is oblique-reverse faulting with a small strike-slip component. The dip angle are high (50° ∼60°) in the proximate of LV but low

(10° ∼15°) at offshore. Therefore we consider the receiver fault angles of (10°, 15°, 80°). The pattern of the ΔCFS values in this region at 25 km depth is given in Figure 5a. Another non-negligible mechanism is N to NNW right lateral strike slips in northern part in Region B (cf. Figure 4) as stated in the previous section. Thus, we also examined the receiver fault angles of (170°, 90°, 180°). The pattern of the ΔCFS values in this region at 15 km depth is positive or neutral except for the southwestern part of Region B, which is stable for the shallow (0∼30 km). The background seismicity in this region, given in Figure 6c, shows slightly increasing activity after 1940's, and we see the steady activity after 1940's as seen in the previous case.

[41] The third region is Taiwan inland, western side of the Longitudinal Valley (LV) included in the regions II and III of Figure 1. Here we assume either thrust type mechanism similar to the Chi-Chi rupture (strike, dip, rake) = (10°, 30°, 60°) or northwest left-lateral strike slip faulting (135°, 90°, 0°) for the transfer faults as described in Section 5. The respective ΔCFS patterns in the depth of 15 km are provided in Figure 5c and d. The stress shadows of the both cases cover the middle latitude area of Taiwan inland (Region C). Also, the stress shadow is shown in the proximity of the LV in the same region due to the high dip angle (50° ∼60°) of the oblique-reverse faulting as described in the above case. The background seismicity in this region given in Figure 6d shows quiet period during 1960-1990, then the recovery of the activity ends up with the occurrence of the Chi-Chi earthquake. It is also seen from the ΔCFS pattern in the depth of 8∼10 km that the assumed aseismic slip could strongly encourage the occurrence of Chi-Chi rupture at the location of its hypocenter. Incidentally, we can clearly see another quiescence during about 15 years period before the Shin-Chu Taichung earthquake (E120.81°, N24.35°, M7.1, 21/Apr/1935), for which we may assume similar scenario.

8 Conclusion

[42] To analyze the seismicity in the Taiwan region, we have applied the space-time ETAS

model, and then the stochastic declustering method that stochastically separates the whole seismicity during the last 100 years into the rates of the background and clustering seismicity rates. Thus, imaging of the separated quantities is performed in order to discuss implication of the regional features of seismicity in and around Taiwan.

[43] The zones of highest background seismicity rates correspond to the zone of high stress accumulation on the tectonic boundaries such as the large transfer fault zones along the eastern part of Longitudinal Valley and northern region of Ryukyu trench beneath which are boundary of Eurasian Plate and subducting Philippine Sea Plate. On the other hand, the regions of the highest clustering seismicity rate correspond to the aftershock area of strong earthquakes. The contrast of above two seismicity rates is enhanced by taking ratio of the clustering seismicity rate to the total seismicity rate (clustering ratio), and its geological interpretation has been discussed in relation to the known major strike-slip faults in Taiwan. In particular, comparison of these data leads to the following remarks: (1) the central-western and the southwestern inland areas have high clustering ratio accompanied by large transfer fault zones, especially for the central-western area. (2) The high clustering ratio area at the eastern offshore has a series of major right-lateral faults. (3) The high clustering ratio of the southeastern offing area may be related to a strike-slip fault trace.

[44] The temporal features of the background seismicity in the central inland regions show conspicuously quiet period up to several decades before the recovery of the activity and then the 1999 Chi-Chi earthquake, while other major seismic regions remain active stationarily. If the principal stress field of each region based on the local tectonic structures prevails the mechanisms of the receiver faults, these difference can be explained by the changes in Coulomb failure stresses caused by the precursory aseismic slips that is assumed to have occurred in an deeper part of the Chi-Chi earthquake fault. From these we can see that only central western Taiwan inland area becomes stress shadow.

9 Acknowledgment

[45] This study was partially supported by A-91-N-FA07-7-4 and Grant-in-aid 1680334. The first author is also supported by JSPS post-doctoral programs. Discussions with Dr. Chang Tsui-Yu, Prof. Ma Kuo-Fong and Prof. Tsai Yi-Ben from the National Central University are helpful.

Reference

Barrier, E., and J. Angelier (1986), Active collision in eastern Taiwan: the Coastal Range, *Tectonophysics*, **125**, 161 – 178.

Console, R., and M. Murru (2001), A simple and testable model for earthquake clustering, *J. Geophys. Res.*, *106*, 8699-8711.

Console, R., M. Murru, and A. M. Lombardi (2003), Refining earthquake clustering models. *J. Geophys. Res.*, *108*(B10), 2468, doi:10.1029/2002JB002130.

Daley, D. and D. Vere-Jones (2003), *An Introduction to Theory of Point Processes*. Spring, New York.

Davis, S. D. and C. Frohlich (1991), Single-linked cluster analysis, synthetic earthquake catalogs, and aftershock identification. *Geophys. J. Int.*, *104*, 289-306.

Deffontaines, B., J. C. Lee, J. Angelier, J. Carvalho And J. P. Rudant (1994), New morphoneotectonic data in Taiwan: analyses of digital elevation model, SPOT and radar images, and geodynamic implications, *J. Geophys. Res.*, *99*, B10: 20,243–20,266.

Deffontaines, B., O. Lacombe, J. Angelier, H. T. Chu, F. Mouthereau, C. T. Lee, J. Deramond, J. F Lee, M. S. Yu and P. M Liew (1997), Quaternary transfer faulting in Taiwan Foothills: evidence from a multisource approach, *Tectonophysics, 274*, 61–82.

Dominguez, S., S. Lallemand, J. Malavieille and P. Schnurle (1998), Oblique subduction of the Gagua Ridge beneath the Ryukyu accretionary wedge system : Insights from marine observations and sandbox experiment, *Mar. Geophys. Res., 20*(5), 383–402.

Frolich, C. and S. D. Davis (1990), Single-linke cluster analysis as a method to evaluate spatial and temporal properties of earthquake catalogs. *Geophys. J. Int.*, *100*, 19-32.

Gardner J. and L. Knopoff (1974), Is the sequence of earthquakes in southern California, with aftershocks removed, Poissonian? *Bull. Seismol. Soc. Am.*, *64*, 1363-1367.

Ho, C. S. (1979), Geologic and tectonic framework of Taiwan, *Mem. Geol. Soc. China, 3*, 57–72.

Ho, C. S. (1986), A synthesis of the geologic evolution of Taiwan, *Tectonophysics, 125*, 1-16.

Hsu, M. T. (1961), Seismicity of Taiwan (Formosa). *Bull. Earthq. Res. Inst., Univ. Tokyo. 39*, 831-847.

Kagan, Y. (1991), Likelihood analysis of earthquake catalogues. *J. Geophys. Res.*, *106, B7*, 135-148.

Kao, H., G. C. Huang and C. S. Liu (2000), Transition from oblique subduction to collision in the northern Luzon arc-Taiwan region: Constrains from bathymetry and seismic observations. *J. Geophys. Res., 105*(B2), 3059–3079.

Kellis-Borok, V. I. and V. I. Kossobokov (1986), Time of increased probability for the great earthquakes of the world. *Computational Seismology*, *19*, 45-58.

Lallemand, S., and C. S. Liu (1998), Geodynamic implications of present-day kinematics in the southern Ryukyus. *J. Geol. Soc. China, 41*, 551–564.

Lallemand, S., C. S. Liu, S. Dominguez, P. Schnurle, and J. Malavieille (1999), The ACT scientific crew, 1999. Trench-parallel stretching and folding of foreare basins and lateral migration of the accretionary wedge in the southern Ryukyu: a case of strain partition caused by oblique convergence. *Tectonics, 18*(2), 231–247.

Lewis P. A. W. and E. Shedler (1979), Simulation of non-homogeneous Poisson processes by thinning. *Naval Res. Logistics Quart.*, *26*, 403-413.

McClay, K. R. (1992), Glossary of thrust tectonic term. In: *Thrust Tectonics*, edited by K.R. McClay, pp. 419-433. Chapman and Hall, London.

MORS (1982), Final report of SLAR survey of the Republic of China. *Mining Research and Service Organization of Industrial Technology Research Institute*, 84 pp.

Musmeci, F. and D. Vere-Jones (1992). A space-time clustering model for historical earthquakes. *Ann. Inst. Stat. Math.*, *44*, 1-11.

Ogata, Y. (1981), On Lewis' simulation method for point processes. *IEEE Translations on Information Theory*, *IT-27*, 23-31.

Ogata, Y. (1988), Statistical model for earthquake occurrences and residual analysis for point processes. *J. Am. Stat. Assoc.*, *83*, 9-27.

Ogata, Y. (1992), Detection of precursory relative quiescence before great earthquakes through a statistical model, *J. Geophys. Res.*, *97*, 19845-19871.

Ogata, Y. (1998), Space-time point-process models for earthquake occurrences, *Ann. Inst. Stat. Math.*, *50*, 379-402.

Ogata, Y. (2004), Space-time model for regional seismicity and detection of crustal stress changes, *J. Geophys. Res.*, *109, B03308*, doi:10.1029/2003JB002621.

Ogata, Y. and J. Zhuang (2004), On space-time ETAS model: an extension. *Res. Memorandom, No ????, the Institute of Statistical Mathematic.*

Omori, F. (1894), On after-shocks of earthquakes. *J. Coll. Sci. Imp. Univ. Tokyo*, *7*, 111-200.

Pelletier, B. and J. F. Stephan (1986), Middle Miocene obduction and late Miocene beginning of collision registered in the Hengchun peninsula: geodynamic implications for the evolution of Taiwan, *Tectonophysics, 125*, 133–160.

Rathbun, S. L. (1993), Modelling marked spatio-temporal point patterns. *Bull. Int. Stat. Inst.*, *55*, Book 2, 379-396.

Resenberg, P. (1985), Second-order moment of Central California Seismicity, 1969 – 1982. *J. Geophys. Res.*, *90, B7*, 5479-5495.

Schnurle, P., C. S. Liu, S. Lallemand, And D. Reed (1998), Structural controls of the Taitung Canyon in the Huatung Basin east of Taiwan, *Terr. Atmos. Oceanic Sci., 9*, 453-473.

Seno, T. (1977), The instantaneous rotation vector of the Philippine Sea plate relative to the Eurasian plate. *Tectonophysics*, *42*, 209-226.

Sun, S.C. (1963), The reef limestones and the geologic structures in the vicinity of Kaohsiung City, Taiwan, *Pet. Geol. Taiwan, 2*, 47–64.

Sun, S.C. (1964), Photogeologic study of the Tainan-Kaohsiung coastal plain area, Taiwan. *Pet. Geol. Taiwan, 3*, 39–51.

Suppe, J. (1980), Imbricated structure of western foothills belt, south-central Taiwan, *Petrol. Geol. Taiwan, 17*, 1–16.

Tsai, Y. B. (1985), A study of disastrous earthquakes in Taiwan, 1683-1895. *Bulletin of Institute of Earth Science, Academia Sinica*, *5*, 1-44.

Tsai, Y. B., (1986), Seismotectonics of Taiwan, *Tectonophysics, 125*, 17–37.

Tsai, Y. B., T. L. Teng, J. M. Chiu, H. L. Liu (1997), Tectonic implications of the seismicity in the Taiwan region, *Mem. Geol. Soc. China, 2*, 13–41.

Utsu, T. (1969), Aftershock and earthquake statistics (I): some parameters which characterize an aftershock sequence and their interrelations. *J. Fac. Sci., Hokkaido University*, *3*, *Ser. VII* (Geophysics), 129-195.

Wang, J. H. and H. C. Kuo (1995) A catalogue of $M_S \geq 7$ Taiwan earthquakes (1900-1994). *J. Geol. Soc. China*, *38*, 95-106.

Wang, J. H. (1998) Studies of earthquake seismology in Taiwan during the 1897-1996 period. *J. Geol. Soc. China*, *41*, 291-336.

Yamanaka, Y. and K. Shimazaki (1990), Scaling relationship between the number of aftershocks and the size of the main shock, *J. Phys. Earth, 38*, 305-324.

Yoshioka, S. (2001), Coseismic slip distribution of the 1999 Chi-Chi, Taiwan, earthquake deduced from inversion analysis of GPS data, *Bull. Seismol. Soc. Am., 91*, 1182-1189.

Yu, S. B., H. Y. Chen, L. C. Kuo (1997), Velocity field of GPS stations in the Taiwan area, *Tectonophysics, 274*, 41-59.

Zhuang, J., Y. Ogata and D. Vere-Jones (2002) Stochastic declustering of space-time earthquake occurrences. *J. Am. Stat. Assoc.*, *97*, 369-380.

Zhuang, J., Y. Ogata and D. Vere-Jones (2004), Analyzing earthquake clustering features by using stochastic reconstruction. *J. Geophys. Res., 109*, B05301, doi:10.1029/2003JB002879.

Table 1: Comparison between the results from fitting Models 1 to 5, to the selected Taiwan data

Model	A	α mag^{-1}	c day	p	D^2 deg^2	q	γ mag^{-1}	$\log L$	AIC
1	0.286	1.103	3.203×10^{-3}	1.067	2.158×10^{-3}	na	na	-2250.8	4513.6
2	0.280	1.326	7.698×10^{-3}	1.086	3.524×10^{-3}	na	na	-3157.9	6327.7
3	0.290	1.112	3.574×10^{-3}	1.072	1.071×10^{-2}	1.705	na	-2226.9	4467.9
4	0.300	1.098	3.600×10^{-3}	1.069	4.603×10^{-3}	1.739	na	-2228.2	4470.3
5	0.277	1.193	3.601×10^{-3}	1.070	7.698×10^{-3}	1.738	0.497	-2224.7	4465.3*

* shows the smallest AIC value.

Figure 1:

Seismotectonic zones of the Taiwan area. CP: Coastal Plain; CeR: Central Range; CoR: Coastal Range; EU: Eurasian plate; HR: Hsüehshan Range; LV: Longitudinal Valley; NLA: northern Luzon volcanic arc; PH: Philippine Sea plate; WF: Western Foothills.

Figure 2:

(a) Epicentral map of the earthquakes. The dashed rectangular represent the study region for the target events (see Section 2.3). (b) Space-time plot of earthquakes with epicenters projected on the line segment AB. Horizontal axis represents the projective distance from A, and vertical axis the occurrence times. (c) Space-time plot of a realization of the background events. See explanation in (b). The arrows indicate the Chi-Chi earthquake.

Figure 3:

Estimated seismicity rate: (a) total seismicity rate $\hat{m}(x, y)$, (b) background seismicity rate $\hat{\mu}(x, y)$, (c) clustering seismicity rate $\hat{C}(x, y)$, and (d) clustering ratio $\Omega(x, y)$; see Equations (20), (22), (24) and (25) for explanation, respectively. The unit for (a) – (c) is $events/(degree^2 \cdot year)$.

Figure 4:

Distribution of seismic clustering ratio (color image) and structural interpretation of the Taiwan area. Red line shows surface faults as interpreted from multi-sources [data after *MORS*, 1982; *Deffontaines et al.*, 1994, 1997; *Lallemand and Liu*, 1998; *Schnurle et al.*, 1998; *Kao et al.*, 2000]. STFZ: Sanyi transfer fault zone; CTFZ: Chiayi transfer fault zone; TCFZ: Taitung Canyon Fault Zone. Details of four areas with high clustering ratio (shown by white frames) are discussed in text.

Figure 5:

Distribution of ΔCFS (color image) in the three typical seismic regions in Taiwan and the vicinity caused by the assumed aseismic slip on the deeper part of the Chi-Chi earthquake fault (see text for the detailed assumptions): (a) far offshore to the northeast of Taiwan Island (Region A) with receiver fault angles of (strike, dip, rake)=(270°, 30°,90°); (b) Eastern offshore region (Region B) to the LV (Longitudinal Valley) with receiver fault angles (10°, 30°, 60°); (c) Central inland region (Region C) with receiver fault angles (10°, 30°, 60°); (d) Central inland region (Region C) as in (c) but with receiver fault angles (135°, 90°, 0°). The scaled numbers are in bars.

Figure 6:

(a) Illustration of regions classified by the tectonics and ΔCFS patterns. The circles represent a stochastic separation of the background events (black circles) and the clustering events (gray circles). Different circle sizes represent the magnitude 5.3 or over. The cumulative curve of background the events in Regions A, B and C are plotted in (b), (c) and (d) in black step functions, respectively. The corresponding cumulative curves of the total events are represented by the gray step functions. The plots of magnitudes against times for each corresponding region are at the bottom of each panel. The arrows indicate the Shin-Chu Taichung earthquake (E120.81°, N24.35°, M7.1, 21/April/1935) and the Chi-Chi earthquake (N120.80°, N23.89°, M7.3, 21/September/1999), respectively.

Figure 1

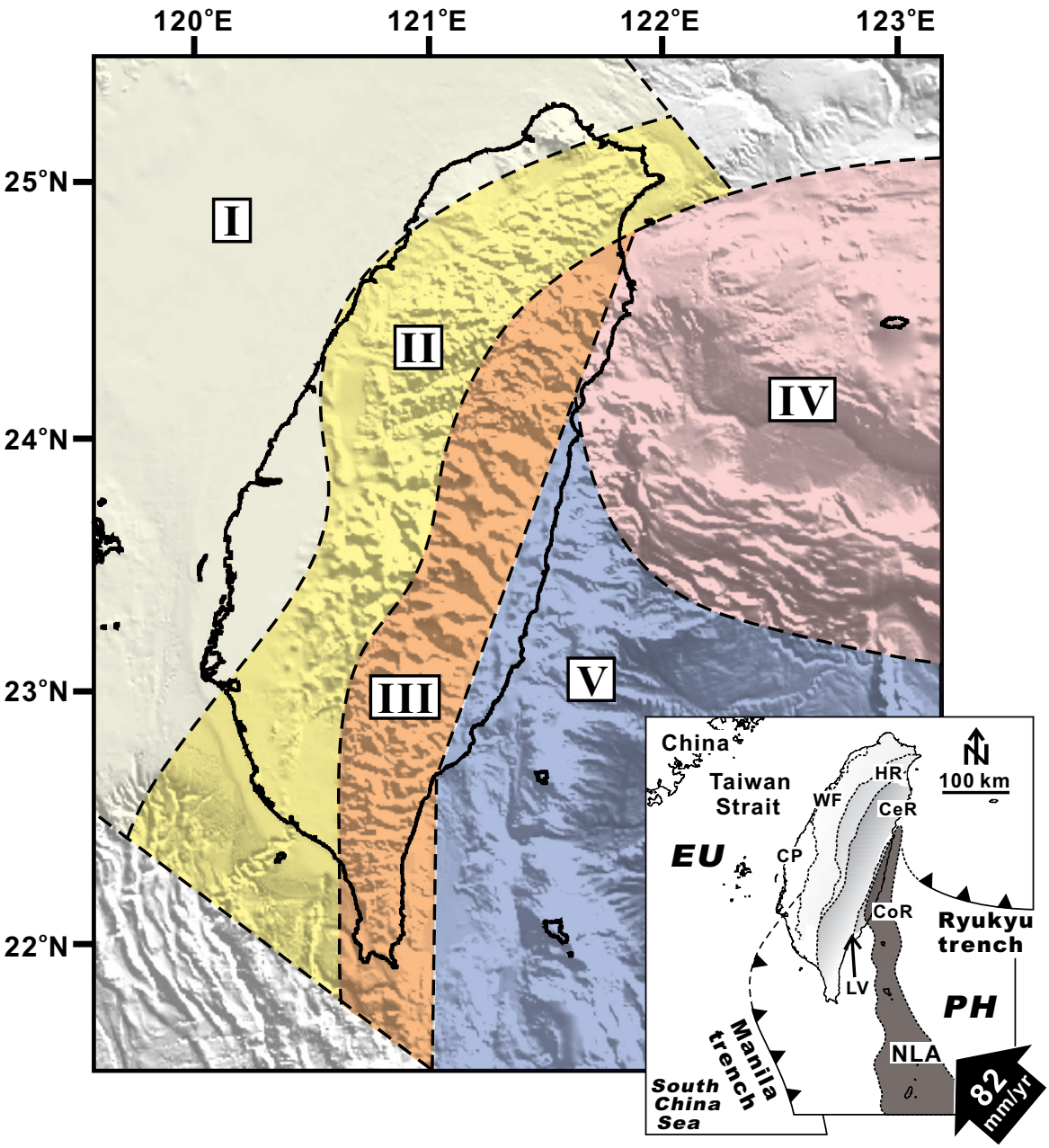
120°E
121°E
122°E
123°E
25°N
24°N
23°N
22°N
I
II
III
IV
V
China
Taiwan
Strait
HR
WF
CeR
CP
EU
CoR
Ryukyu
trench
LV
PH
NLA
Manila
trench
South
China
Sea
82
mm/yr
N
100 km

Figure 2

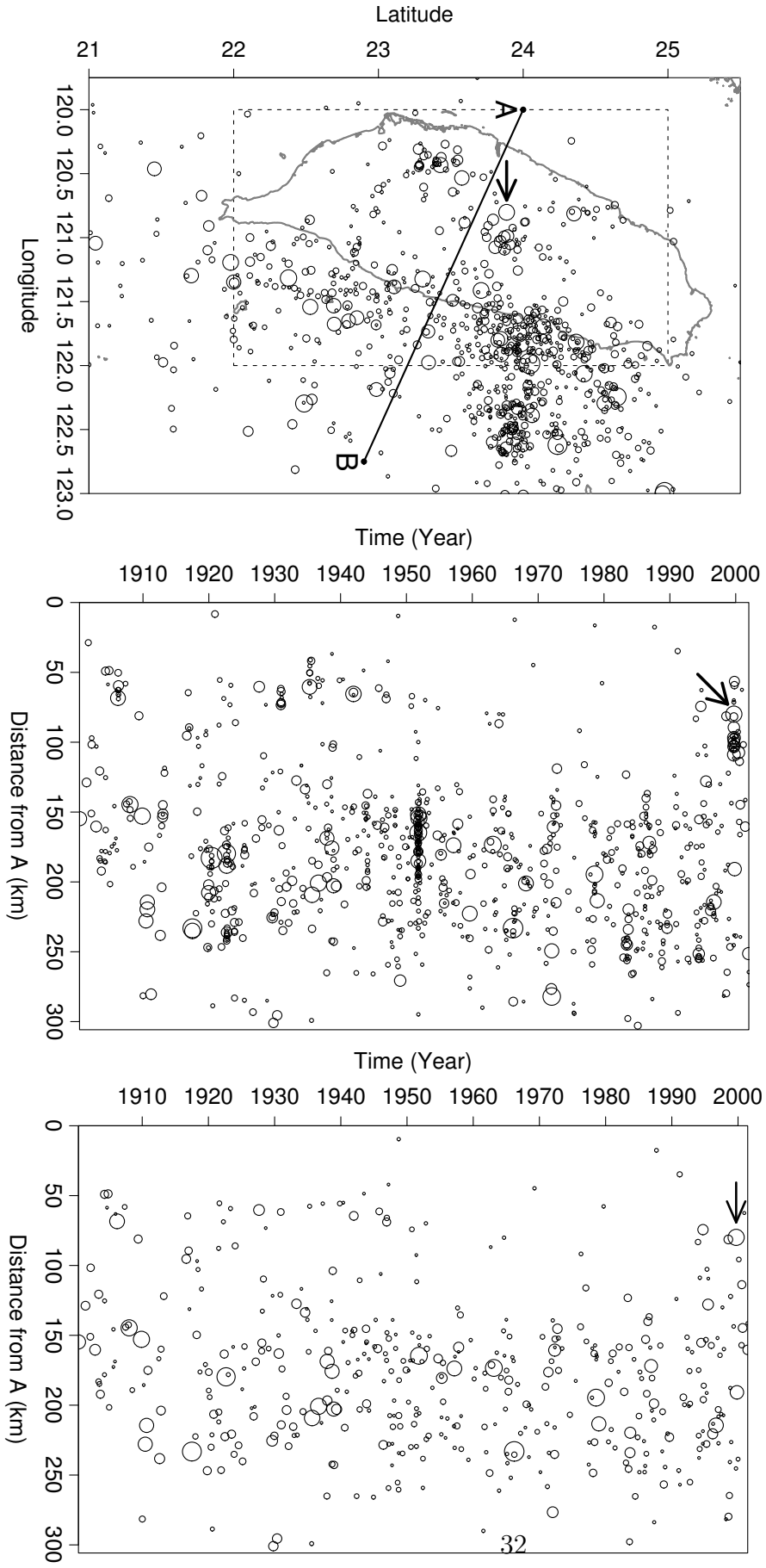
Latitude
21
22
23
24
25
Longitude
120.0
120.5
121.0
121.5
122.0
122.5
123.0
A
B
Time (Year)
1910
1920
1930
1940
1950
1960
1970
1980
1990
2000
Distance from A (km)
0
50
100
150
200
250
300
Time (Year)
1910
1920
1930
1940
1950
1960
1970
1980
1990
2000
Distance from A (km)
0
50
100
150
200
250
300

Figure 3

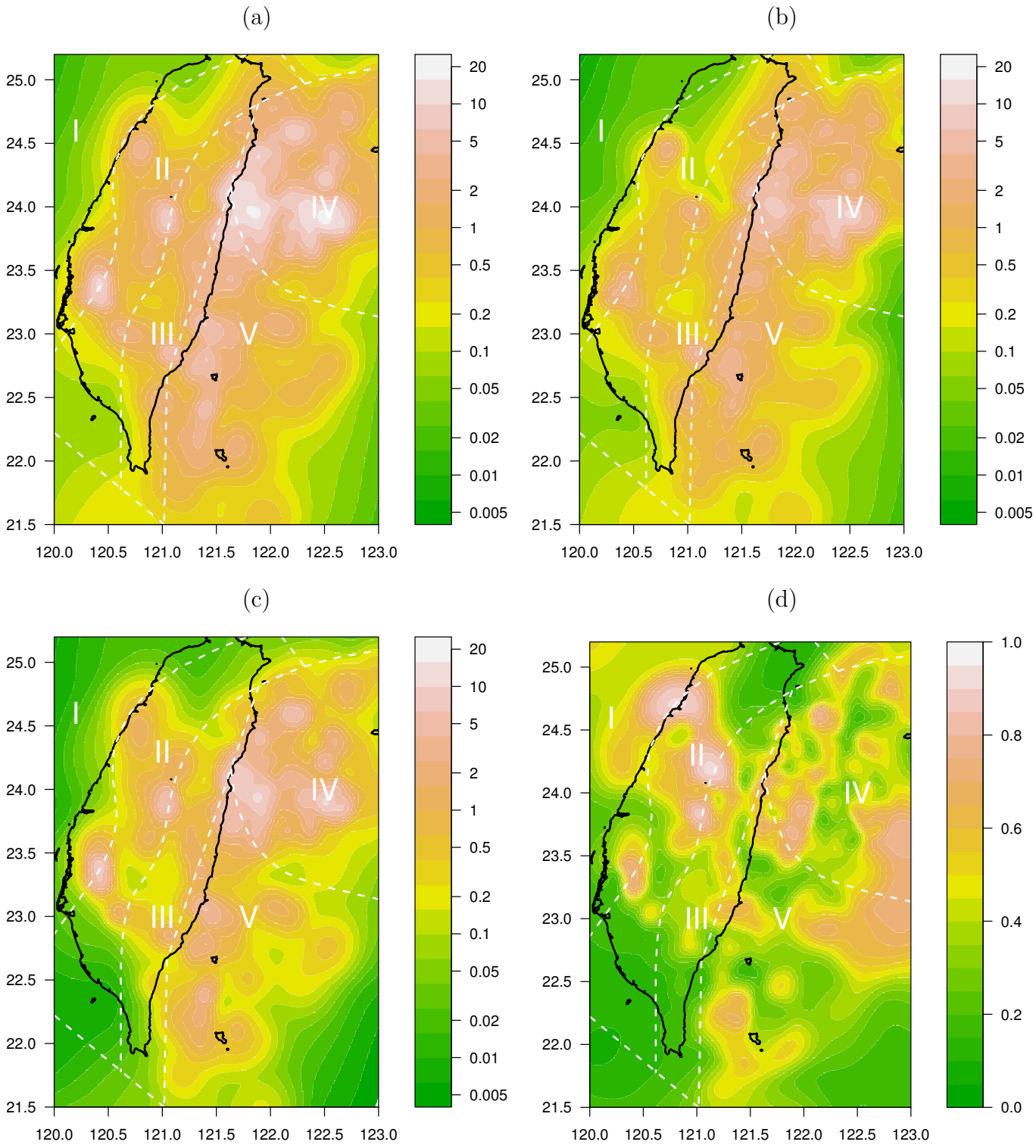
(a)
(b)
(c)
(d)
I
II
III
IV
V
25.0
24.5
24.0
23.5
23.0
22.5
22.0
21.5
120.0
120.5
121.0
121.5
122.0
122.5
123.0
20
10
5
2
1
0.5
0.2
0.1
0.05
0.02
0.01
0.005
1.0
0.8
0.6
0.4
0.2
0.0

Figure 4

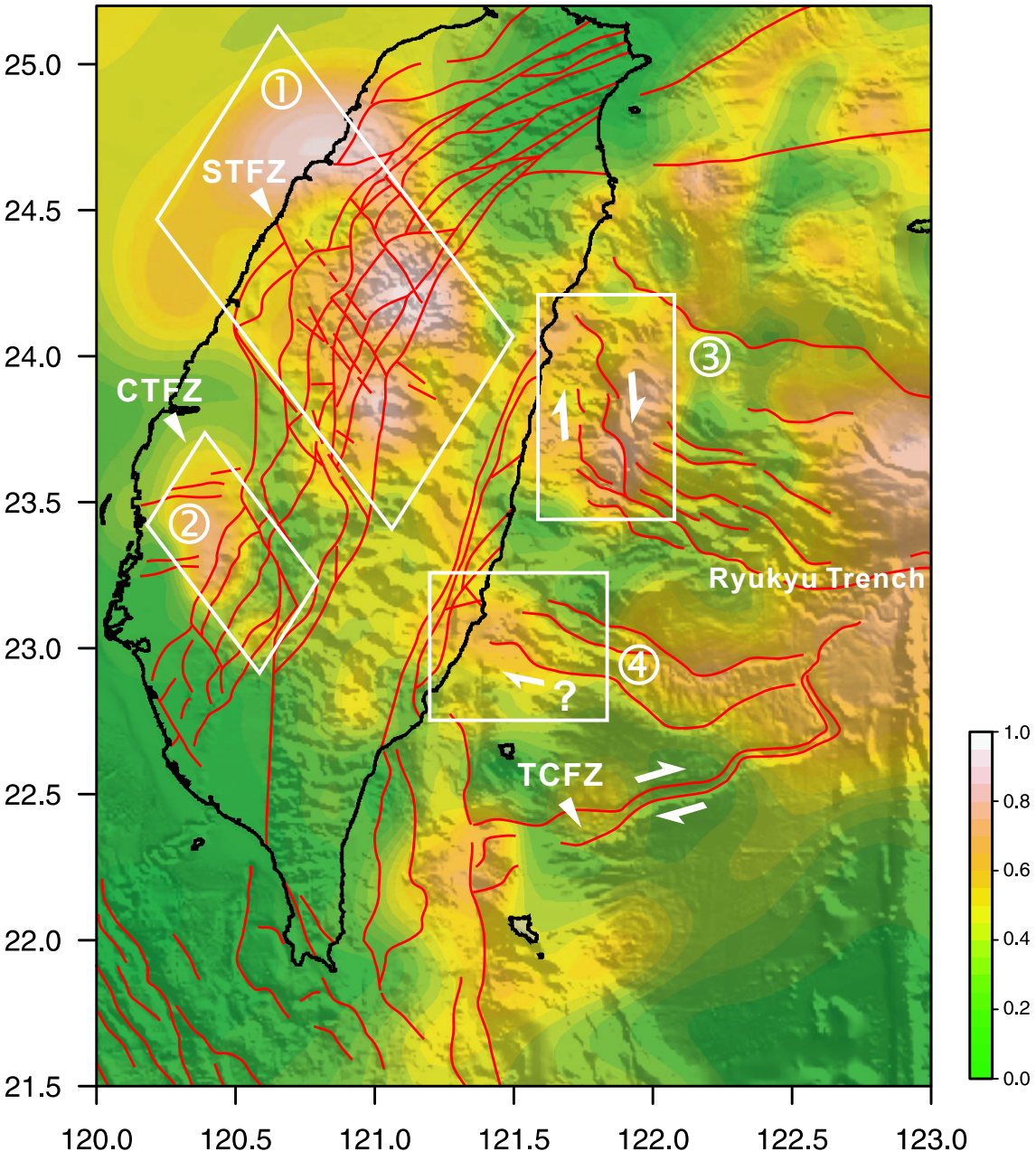
①
STFZ
②
CTFZ
③
1
④
?
Ryukyu Trench
TCFZ
25.0
24.5
24.0
23.5
23.0
22.5
22.0
21.5
120.0
120.5
121.0
121.5
122.0
122.5
123.0
1.0
0.8
0.6
0.4
0.2
0.0

Figure 5

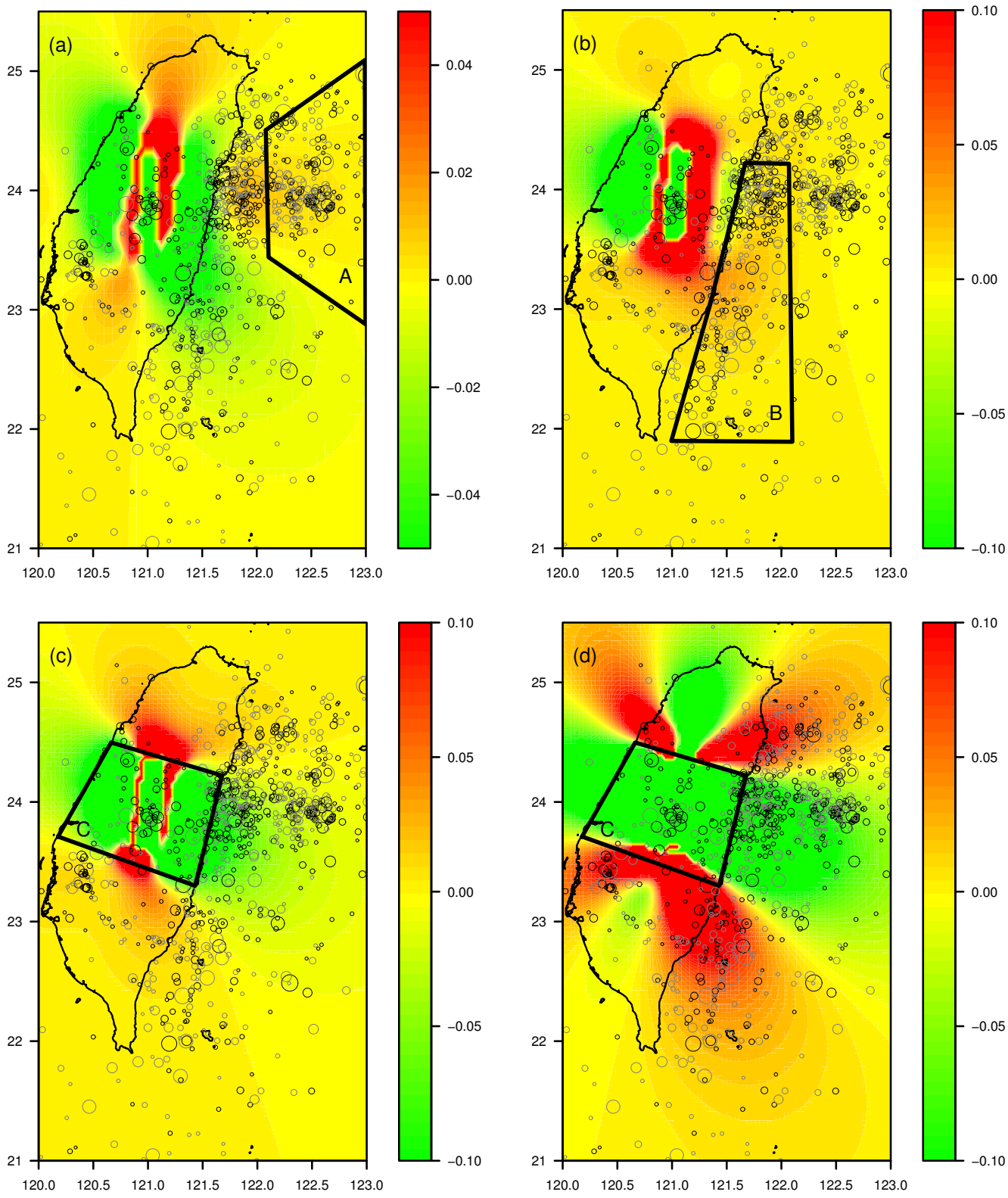
(a)
A
(b)
B
(c)
C
(d)
C
25
24
23
22
21
120.0
120.5
121.0
121.5
122.0
122.5
123.0
0.04
0.02
0.00
−0.02
−0.04
0.10
0.05
0.00
−0.05
−0.10

Figure 6

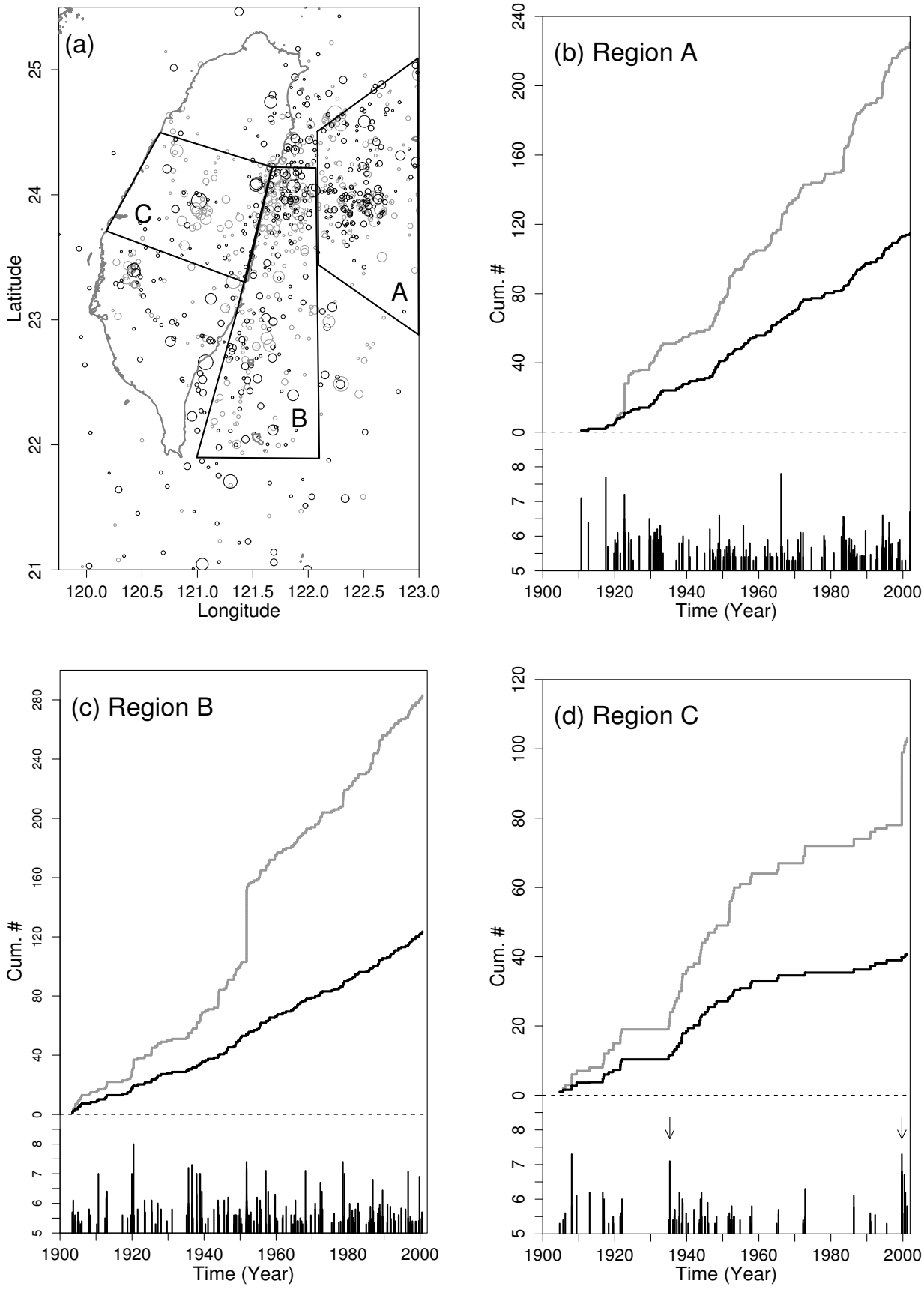
(a)
Latitude
Longitude
120.0 120.5 121.0 121.5 122.0 122.5 123.0
21 22 23 24 25
A
B
C
(b) Region A
Cum. #
Time (Year)
1900 1920 1940 1960 1980 2000
(c) Region B
(d) Region C